Optics & Laser Technology 164 (2023) 109493

Contents lists available at ScienceDirect

Optics and Laser Technology

journal homepage: www.elsevier.com/locate/optlastec

Full length article

Polarization insensitive metamaterial engineered multimode interference coupler in a 220 nm silicon-on-insulator platform

Carlos Pérez-Armenta [a,*], Alejandro Ortega-Moñux [a], José Manuel Luque-González [a], Robert Halir [a], Jens Schmid [b], Pavel Cheben [b], Iñigo Molina-Fernández [a], J. Gonzalo Wangüemert-Pérez [a]

[a] Telecommunication Research Institute (TELMA), Universidad de Málaga, CEI Andalucía TECH, E.T.S.I. Telecomunicación, 29010 Málaga, Spain
[b] National Research Council Canada, Ottawa, Ontario K1A 0R6, Canada

ARTICLE INFO

Keywords:
Silicon photonics
Silicon-on-insulator
Subwavelength gratings
Multimode interference
Polarization insensitivity

ABSTRACT

High-index contrast silicon waveguides exhibit strong birefringence that hinders the development of polarization-insensitive devices, especially for sub-micrometer silicon layer thickness. Here a polarization-independent 2 × 2 multimode interference coupler in a 220 nm silicon-on-insulator platform is designed and experimentally demonstrated for the first time. Leveraging the advanced control of electromagnetic properties provided by a subwavelength grating metamaterial topology, our multimode interference coupler operates for both TE and TM polarization states with measured polarization dependent loss, insertion loss and imbalance all less than 1 dB, and phase errors below 5° in the wavelength range from 1500 nm to 1560 nm. The device has a footprint of only 3.5 μm × 47.25 μm and was fabricated using a single etch-step process with a minimum feature size of 100 nm compatible with immersion deep-UV lithography.

1. Introduction

Silicon-on-insulator (SOI) is a well-established platform for implementing advanced photonic integrated circuits (PICs) [1]. The high index contrast of SOI and the mature CMOS-compatible manufacturing processes enable the fabrication of compact and low-cost photonic systems such as datacom and telecom transceivers [2], biochemical sensors [3], programmable photonic processors [4], optical phased arrays [5] and quantum photonic devices [6], to name a few. Multimode interference couplers (MMIs) are fundamental building blocks in these systems, providing large operational bandwidths and a good tolerance to fabrication errors [7]. However, SOI MMIs employ highly birefringent waveguides, particularly in the multimode region, typically optimized only for the transverse electric (TE) modes, hampering the realization of polarization-agnostic devices.

Polarization insensitivity is required in applications that use polarization multiplexing or operate with light in a random state of polarization [8]. One strategy for developing polarization-independent PICs is polarization diversity [9]. However, it usually requires almost twice the chip area and introduces additional insertion loss due to polarization splitters, rotators, and combiners. While square cross-section waveguides can be used to achieve zero-birefringence operation [10], this is not applicable in MMIs as they require a wide multimode waveguide. Polarization independence can also be achieved by using a particular multimode waveguide width for which TE and TM modes beat lengths are equal [11]. However, this strategy works only for silicon thicknesses above 300 nm [11], requiring new design approaches to achieve polarization insensitivity in standard 220-nm-thick SOI platform.

Since their first demonstration in silicon photonics [12,13], SWG metamaterials have been extensively used to engineer both the refractive index and dispersion of silicon waveguides [14,15]. SWG structures have been successfully implemented to develop new types of waveguide crossings and MMI couplers [16,17,18]. Furthermore, the unique properties of SWGs have enabled the development of polarization management components such as polarization beam splitters [19,20], polarization-dependent Bragg grating filters [21] and polarizers [22]. SWG-engineered polarization-insensitive devices have also been demonstrated, including fiber-to-chip edge couplers [23], directional couplers [24], power splitters [25,26] and tilted non-birefringent waveguides [27].

Here we experimentally demonstrate, for the first time to the best of

* Corresponding author.
E-mail address: cpa@ic.uma.es (C. Pérez-Armenta).

https://doi.org/10.1016/j.optlastec.2023.109493
Received 8 November 2022; Received in revised form 24 January 2023; Accepted 11 April 2023
Available online 25 April 2023

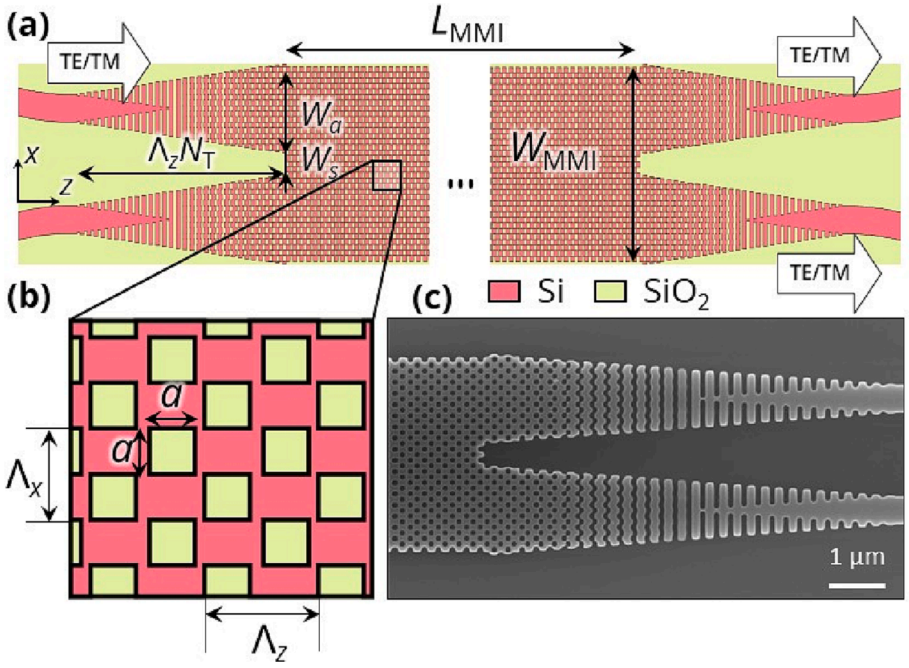

Fig. 1. (a) Top view of the designed MMI device. (b) Proposed metamaterial multimode waveguide. (c) SEM image of the fabricated MMI prior to the deposition of the SiO_2 top cladding.

our knowledge, a polarization independent 2 × 2 MMI coupler fabricated on a conventional 220-nm SOI platform using a single full-etch step process. The device is based on a 2D periodic SWG metamaterial to achieve polarization agnostic performance in the wavelength range from 1500 to 1560 nm while maintaining a minimum feature size of 100 nm compatible with deep-UV lithography.

2. Working principle and design

The device geometry is shown schematically in Fig. 1(a). It consists of a metamaterial multimode waveguide and transition tapers between conventional silicon wire interconnecting waveguides and SWG input/output access ports. As depicted in Fig. 1(b), the SWG pattern is periodic in x and z directions with periods Λ_x and Λ_z, respectively. The periodicities are created by interlacing silicon dioxide square holes of size $a \times a$ in a solid silicon waveguide core. The chessboard topology allows us to achieve polarization insensitivity using a simplified design process compared to generic bricked nanostructure based on variable longitudinal shifting [28]. The width and length of the multimode waveguide are W_{MMI} and $L_{MMI} = \Lambda_z N_{MMI}$, respectively, where N_{MMI} is the number of periods of the periodic MMI core in the propagation direction. The refractive indices of Si and SiO_2 are 3.476 and 1.444 at $\lambda = 1550$ nm, respectively.

Adiabatic transitions are used to adapt the silicon wire and SWG fundamental modes and to widen the access waveguides so the number of modes excited in the multimode region is restricted [29]. The transition comprises N_T periods distributed over two sections with equal number of periods ($N_T/2$). The first section converts the silicon wire into a conventional z-periodic SWG waveguide with period Λ_z while the second one introduces the x-periodicity by progressively shifting half of the SWG strips to achieve the proposed topology. This strategy also reduces possible Bragg reflections [28]. Both taper sections are linearly widened from the interconnection waveguide width of 500 nm to the access port width W_a, with the access ports being separated by a gap W_s.

From self-imaging theory, it is possible to obtain the distance where the first two-fold image of an arbitrary input field profile is formed [7]

$$L_{MMI} = \frac{3\lambda}{4\left(n_{eff}^{(0)} - n_{eff}^{(1)}\right)} \tag{1}$$

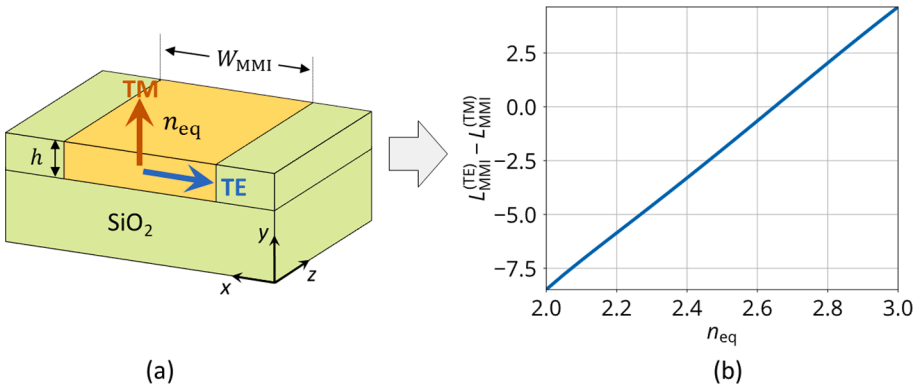

Fig. 2. (a) Equivalent strip waveguide with a homogeneous core material synthesized by using the chessboard patterned SWG metamaterial. (b) MMI length difference for TE and TM polarizations as a function of the equivalent refractive index n_{eq}.

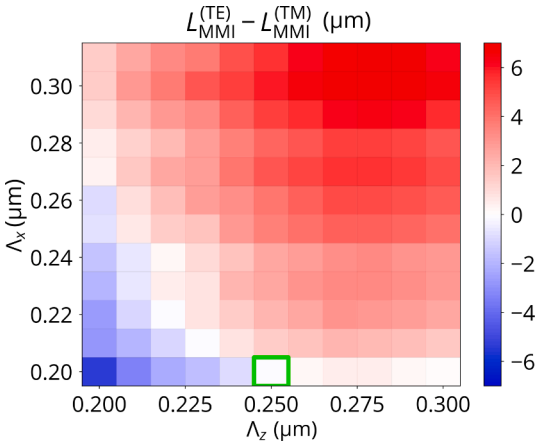

Fig. 3. Difference between MMI lengths for TE and TM polarizations, and different periods Λ_x and Λ_z, $a = 100$ nm, $W_{MMI} = 3.5$ μm, $h = 220$ nm, $\lambda = 1550$ nm. Nominal design is marked in green. (For interpretation of the references to colour in this figure legend, the reader is referred to the web version of this article.)

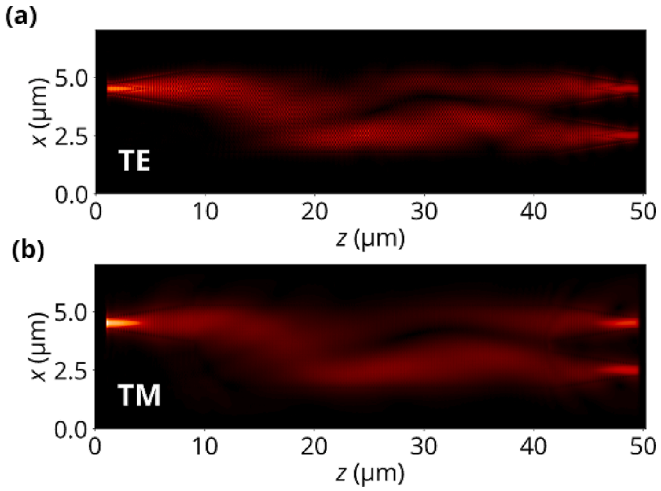

Fig. 4. (a) $|E_x|$ field component of TE mode and (b) $|E_y|$ field component of TM mode propagation along the MMI obtained by a 3D FDTD simulations for$\lambda = 1550$ nm.

where $n_{eff}^{(i)}$ is the effective index of the i-th mode for a given polarization. Ideally, a 2 × 2 MMI with length given by Eq. (1) equally splits the power entering by any input port with a relative phase shift of 90°. For polarization insensitive operation, MMI lengths for TE and TM polarizations must match, i.e., $L_{MMI}^{(TE)} = L_{MMI}^{(TM)}$. Although this condition cannot be fulfilled using a 220 nm-thick solid-core multimode region, a judicious design of the SWG metamaterial of Fig. 1(b) overcomes this limitation, finally achieving a polarization agnostic device.

We model the SWG multimode region as an equivalent homogeneous metamaterial with refractive index n_{eq}, as depicted in Fig. 2(a). The MMI width is set to $W_{MMI} = 3.5$ μm, which yields good optical imaging properties (4 or more guided modes for both polarizations) and compact design. Based on this approximate model, we calculated the difference between the MMI lengths for TE and TM polarizations as a function of n_{eq}. As shown in Fig. 2(b), polarization insensitivity is achieved for an equivalent metamaterial index $n_{eq} = 2.65$ and the estimated MMI length is 34 μm. These calculations confirm that a polarization independent MMI can be obtained using a judiciously designed SWG metamaterial for the multimode region, as shown in Fig. 1(b). The geometrical parameters of the SWG region (a, Λ_x and Λ_z) are determined as follows: We first impose a hole size of $a = 100$ nm to ensure fabricability. The MMI width is set to $W_{MMI} = 3.5$ μm, as a compromise for good optical imaging (enough guided modes) and compact design. Then, we optimize the pitches Λ_x and Λ_z to minimize the absolute value of the MMI polarization length difference $\Delta L(\Lambda_x, \Lambda_z) = L_{MMI}^{(TE)} - L_{MMI}^{(TM)}$, while ensuring a minimum feature size of 100 nm and avoiding the Bragg regime. Note that an estimate of ΔL can be obtained with a reduced computational cost using Eq. (1) and the MPB solver [30] to calculate the first two TE and TM modes of the periodic multimode waveguide.

Fig. 3 shows $L_{MMI}^{(TE)} - L_{MMI}^{(TM)}$ for sweeping the periods Λ_x and Λ_z, revealing multiple solutions satisfying the polarization independence condition. Our nominal design is marked in green, corresponding to $\Lambda_x = 200$ nm, $\Lambda_z = 250$ nm and $L_{MMI} = 32$ μm, for $W_{MMI} = 3.5$ μm and $a = 100$ nm. In this design, we opted for a minimum feature size of 100 nm, to ensure that the SWG operates far enough from the Bragg regime within the full wavelength range. Other designs with larger feature sizes are possible at the cost of a reduced bandwidth, limited by the proximity of the bandgap at shorter wavelengths.

Then, the full device shown in Fig. 1(a) is simulated using the 3D FDTD simulator Meep [31], yielding the S-parameters of the full 4-port structure. The access ports taper dimensions are $W_a = 1.6$ μm, $W_s = 400$ nm, and $N_T = 30$. A small tuning of the number of periods in the z-direction of the MMI region is performed at this stage, finally obtaining $N_{MMI} = 129$ ($L_{MMI} = 32.25$ μm). Fig. 4 (a) and (b) show the TE and TM fields evolution, respectively, when one of the input ports is excited using a continuous wave source with a wavelength of $\lambda = 1550$ nm. It is clearly observed that the distance at which the double image is formed is identical for both polarizations, yielding polarization agnostic performance.

3. Fabrication and experimental characterization

The test structures were fabricated on an SOI platform with a 220 nm-thick silicon layer and a 2 μm-thick buried oxide (BOX). Samples were patterned using electron beam lithography and then etched via anisotropic inductively coupled plasma reactive ion etching. A 2.2 μm SiO_2 layer was deposited as the upper cladding. Fig. 1(c) shows a scanning electron microscope (SEM) image of the multimode waveguide and the output section of the fabricated MMI before the cladding deposition. To characterize the device, unbalanced Mach-Zehnder interferometers (MZI) were fabricated incorporating two identical MMIs as power splitters. The length difference between the MZI arms was 100 μm, corresponding to a free spectral range of 5 and 7 nm for TE and TM polarizations, respectively. Individual MMIs were also included on the chip to characterize the fabricated structures. Linearly polarized light from a tunable semiconductor laser was coupled to the chip using a lensed fiber and a broadband polarization-independent SWG edge coupler [23]. A fiber polarization controller was used to select the input polarization state. On the chip, the light was guided to the set of test structures, including the individual MMIs and unbalanced MZIs. Both outputs of MMI devices were routed to the chip edge and connected to SWG metamaterial output edge couplers. The light exiting the chip was collimated by a microscope objective, filtered by a Glan-Thompson polarizer, and intercepted by a germanium photodetector connected to a digital power meter.

Several test structures were included in the fabricated chip with small variations in the geometrical parameters to compensate possible fabrication errors in the silicon layer thickness, MMI width, hole types and dimensions, and the effect of voids [32,18]. To estimate different types of design flavors to be included in the layout, we studied the variation in the number of periods of the MMI for an in-plane etching error of $\delta = \pm 5$ nm, as well as the case of the holes not filled with SiO_2 cladding, as shown in Fig. 5. The results of this analysis are summarized in Table 1. It is observed that TE modes are more sensitive to fabrication errors compared to TM modes, and that tolerance to etching error can be

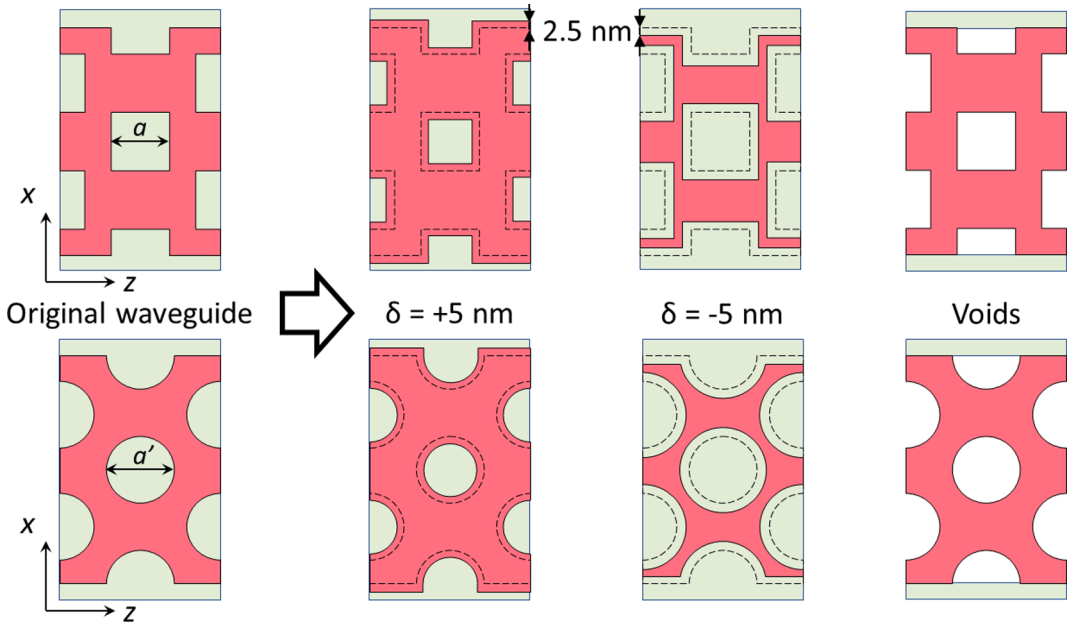

Fig. 5. Fabrication tolerances: The effect of etching error δ and air voids (holes not filled with the SiO_2 cladding).

Table 1
Variation of the number of periods for the nominal design, for etching errors $\delta = \pm 5$ nm and air voids.

	ΔN_{MMI}					
	$\delta = +5$nm		$\delta = -5$nm		Voids	
	TE	TM	TE	TM	TE	TM
Square holes ($a = 100$ nm)	4	<1	−8	<1	−5	1
Circular holes ($a' = 113$ nm)	4	<0.1	−3	<0.1	−5	1

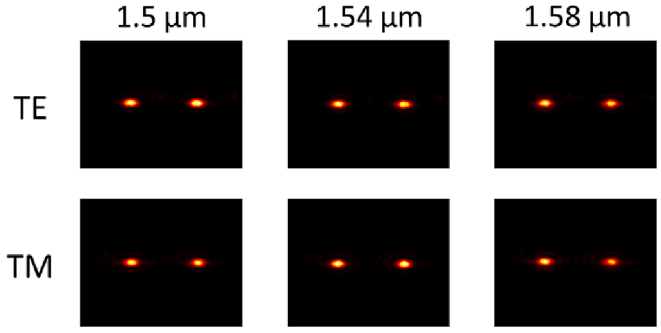

Fig. 6. Pseudocolor images of the outputs of a fabricated polarization independent MMI with $N_{MMI} = 135$, as captured with a SWIR camera.

increased by using circular holes instead of square topology. The best performance was obtained for the nominal design just with a small adjustment of 6 additional periods (1.6 μm) in the multimode region length, i.e., for $N_{MMI} = 135$. Fig. 6 shows the light at the outputs of an individual MMI captured with a SWIR camera for both polarizations and three different wavelengths, confirming the good performance of the MMI. The measured transmittances of each output of an MZI are shown in Fig. 7 for both polarizations (solid curves). Blue curves correspond to output port A in the inset of Fig. 7 and red curves correspond to output port B. The transmittance was obtained normalizing the measured output power to a reference test waveguide, thus calibrating out the

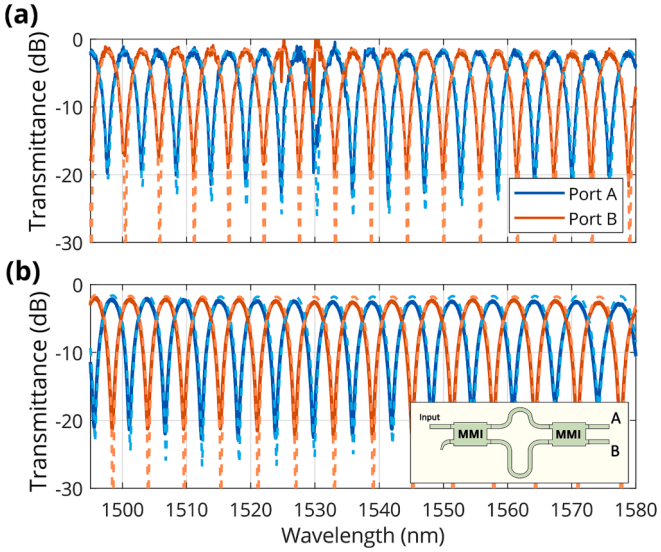

Fig. 7. Measured (solid curves) and modelled (dashed curves) transmittance of the two outputs of the unbalanced MZI (inset) for (a) TE and (b) TM polarizations.

input and output coupling losses and the waveguide propagation loss. A distorted transmittance is observed for TE polarization in the wavelength range 1525–1535 nm. This is due to a fabrication glitch which affected this specific batch, resulting in a transmittance dip for the interconnecting Si-wire waveguides near 1530 nm for TE polarization.

To evaluate the performance of the fabricated MMIs, we used the following analytical model of an unbalanced MZI with two identical non-ideal 2 × 2 MMIs. The transmittances of the MZI output ports A and B (as schematically shown in the inset of Fig. 7(b)) are given by [33]:

$$T_A = |S_{21}|^4 + |S_{31}|^4 - 2|S_{21}|^2|S_{31}|^2\cos(2\,\mathrm{PE} - \Delta\phi) \quad (2)$$

$$T_B = 2|S_{21}|^2|S_{31}|^2\,[1 + \cos\Delta\phi] \quad (3)$$

where S_{ij} are the S-parameters of the MMI, $\mathrm{PE} = \angle(S_{31}/S_{21}) - 90^\circ$ is the phase error and $\Delta\phi = 2\pi n_{\mathrm{eff}}\Delta L/\lambda$ is the phase difference between the

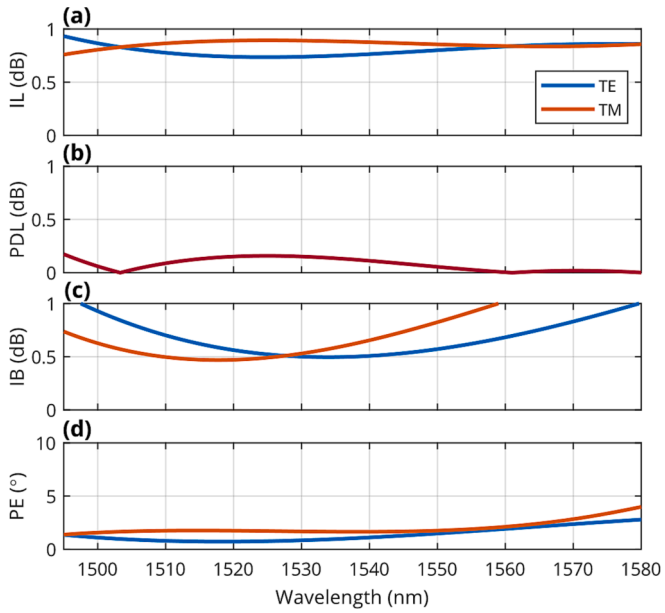

Fig. 8. MMI figures of merit extracted from the measured interferograms shown in Fig. 7: (a) insertion loss, (b) polarization dependent loss, (c) imbalance and (d) phase error.

MZI arms. Following the methodology outlined in [33], the S-parameters of the MMI are obtained and the figures of merit are calculated, including: the phase error; the insertion loss, $\mathrm{IL} = -10\log_{10}\left(|S_{21}|^2 + |S_{31}|^2\right)$; and the imbalance, $\mathrm{IB} = 10\log_{10}\left(|S_{31}|^2/|S_{21}|^2\right)$. The calculated IL, IB and PE are shown in Fig. 8 along the polarization dependent loss $\mathrm{PDL} = |\mathrm{IL_{TE}} - \mathrm{IL_{TM}}|$. The modelled transmittances of the MZI obtained from introducing the calculated figures of merit in Eqs. (2) and (3) are shown in Fig. 7 (dashed curves). It is observed that the MMI exhibits insertion loss between 0.7 and 1 dB, yielding a PDL of less than 0.25 dB in the measured wavelength range (1495 nm – 1580 nm). The MMI imbalance is less than 1 dB from 1500 nm to 1560 nm and the phase error is below 5° over the entire measurement bandwidth. Except for the imbalance, which limits the bandwidth to 60 nm, both polarizations behave very similarly and have good performance in the entire measured wavelength range (85 nm).

4. Conclusions

We designed, fabricated and experimentally characterized a polarization-agnostic 2 × 2 3 dB 90° MMI coupler for the 220 nm SOI platform and C-band operation. The polarization independent operation was achieved through waveguide birefringence engineering using a SWG metamaterial topology. Our MMI device has a footprint of only 3.5 μm × 47.25 μm and was fabricated using a single etch-step process with a minimum feature size of 100 nm. It has the insertion loss and imbalance below 1 dB, polarization dependent loss under 0.25 dB and phase errors of less than 5° in a 60 nm bandwidth. The results demonstrated in this work can be extended to MMI couplers with an arbitrary number of ports and open the way towards the development of high-performance polarization independent silicon photonic components leveraging periodic SWG topologies.

CRediT authorship contribution statement

Carlos Pérez-Armenta: Conceptualization, Formal analysis, Investigation, Visualization, Writing – original draft. **Alejandro Ortega-Moñux:** Conceptualization, Supervision, Formal analysis, Writing – review & editing, Project administration. **José Manuel Luque-González:** Conceptualization, Formal analysis. **Robert Halir:** Resources, Writing – review & editing. **Jens Schmid:** Writing – review & editing. **Pavel Cheben:** Conceptualization, Supervision, Writing – review & editing. **Iñigo Molina-Fernández:** Conceptualization, Project administration, Resources, Funding acquisition. **J. Gonzalo Wangüemert-Pérez:** Conceptualization, Supervision, Writing – review & editing.

Declaration of Competing Interest

The authors declare that they have no known competing financial interests or personal relationships that could have appeared to influence the work reported in this paper.

Data availability

Data will be made available on request.

Acknowledgements

We acknowledge funding from Ministerio de Economía y Competitividad (PID2019106747RB-I00), Junta de Andalucía (P18-RT-1453, UMA-FEDERJA-158), Ministerio de Ciencia, Innovación y Universidades (FPU16/06762, FPU19/02408), and Universidad de Málaga. Funding for open access charge: Universidad de Málaga / CBUA.

References

[1] A. Rahim, T. Spuesens, R. Baets, W. Bogaerts, Open-Access Silicon Photonics: Current Status and Emerging Initiatives, Proceedings of the IEEE 106 (12) (2018) 2313–2330. doi: https://doi.org/10.1109/JPROC.2018.2878686.
[2] R. Sabella, Silicon Photonics for 5G and Future Networks, IEEE J. Sel. Top. Quantum Electron. 26 (2) (2020) 1–11, https://doi.org/10.1109/JSTQE.2019.2948501.
[3] E. Luan, H. Shoman, D.M. Ratner, K.C. Cheung, L. Chrostowski, Silicon photonic biosensors using label-free detection, Sensors 18 (10) (2018) 3519, https://doi.org/10.3390/s18103519.
[4] W. Bogaerts, D. Perez, J. Capmany, D.A.B. Miller, J. Poon, D. Englund, F. Morichetti, A. Melloni, Programmable photonic circuits, Nature 586 (7828) (2020) 207–216, https://doi.org/10.1038/s41586-020-2764-0.
[5] C. Rogers, A.Y. Piggott, D.J. Thomson, R.F. Wiser, I.E. Opris, S.A. Fortune, A. J. Compston, A. Gondarenko, F. Meng, X. Chen, G.T. Reed, R. Nicolaescu, A universal 3D imaging sensor on a silicon photonics platform, Nature 590 (7845) (2021) 256–261, https://doi.org/10.1038/s41586-021-03259-y.
[6] J. Wang, F. Sciarrino, A. Laing, M.G. Thompson, Integrated photonic quantum technologies, Nat. Photonics 14 (5) (2020) 273–284, https://doi.org/10.1038/s41566-019-0532-1.
[7] L.B. Soldano, E.C. Pennings, Optical Multi-Mode Interference Devices Based on Self-Imaging: Principles and Applications, J. Lightwave Technol. 13 (4) (1995) 615–627, https://doi.org/10.1109/50.372474.
[8] D. Dai, L. Liu, S. Gao, D.X. Xu, S. He, Polarization management for silicon photonic integrated circuits, Laser Photonics Rev. 7 (3) (2013) 303–328, https://doi.org/10.1002/lpor.201200023.
[9] T. Barwicz, M.R. Watts, M.A. Popovic, P.T. Rakich, L. Socci, F.X. Kartner, E. P. Ippen, H.I. Smith, Polarization-transparent microphotonic devices in the strong confinement limit, Nat. Photonics 1 (1) (2007) 57–60, https://doi.org/10.1038/nphoton.2006.41.
[10] S.T. Lim, C.E. Png, E.A. Ong, Y. Long Ang, Single mode, polarization-independent submicron silicon waveguides based on geometrical adjustments, Opt. Express 15 (18) (2007) 11061–11072, https://doi.org/10.1364/OE.15.011061.
[11] D. Dai, S. He, Optimization of ultracompact polarization-insensitive multimode interference couplers based on Si nanowire waveguides, IEEE Photon. Technol. Lett. 18 (19) (2006) 2017–2019. doi: https://doi.org/10.1109/LPT.2006.882227.
[12] P. Cheben, S. Janz, D. Xu, B. Lamontagne, A. Delage, S. Tanev, A broad-band waveguide grating coupler with a subwavelength grating mirror, IEEE Photon. Technol. Lett. 18 (1) (2006) 13–15, https://doi.org/10.1109/LPT.2005.860037.
[13] P. Cheben, P.J. Bock, J.H. Schmid, J. Lapointe, S. Janz, D.-X. Xu, A. Densmore, A. Delage, B. Lamontagne, T.J. Hall, Refractive index engineering with subwavelength gratings for efficient microphotonic couplers and planar waveguide multiplexers, Opt. Lett. 35 (15) (2010) 2526, https://doi.org/10.1364/ol.35.002526.
[14] P. Cheben, R. Halir, J.H. Schmid, H.A. Atwater, D.R. Smith, Subwavelength integrated photonics, Nature 560 (7720) (2018) 565–572, https://doi.org/10.1038/s41586-018-0421-7.
[15] J. M. Luque-Gonzalez, A. Sánchez-Postigo, A. Hadij-Elhouati, A. Ortega- Moñux, J. G. Wangüemert-Pérez, J. H. Schmid, P. Cheben, I. Molina- Fernández, R. Halir, A review of silicon subwavelength gratings: Building break-through devices with anisotropic metamaterials, Nanophotonics 10 (11) (2021) 2765–2797. doi: https://doi.org/10.1515/nanoph-2021-0110.

[16] P.J. Bock, P. Cheben, J.H. Schmid, J. Lapointe, A. Delage, D.-X. Xu, S. Janz, A. Densmore, T.J. Hall, Subwavelength grating crossings for silicon wire waveguides, Opt. Express 18 (15) (2010) 16146–16155, https://doi.org/10.1364/OE.18.016146.

[17] W. Chang, L. Lu, X. Ren, D. Li, Z. Pan, M. Cheng, D. Liu, M. Zhang, Ultracompact dual-mode waveguide crossing based on subwavelength multimode-interference couplers, Photon. Res. 6 (7) (2018) 660–665, https://doi.org/10.1364/PRJ.6.000660.

[18] R. Halir, P. Cheben, J. M. Luque-González, J. D. Sarmiento-Merenguel, J. H. Schmid, J. G. Wangüemert-Pérez, D. X. Xu, S. Wang, A. Ortega- Moñux, I. Molina-Fernández, Ultra-broadband nanophotonic beamsplitter using an anisotropic sub-wavelength metamaterial, Laser and Photonics Reviews 10 (6) (2016) 1039–1046. doi: https://doi.org/10.1002/lpor.201600213.

[19] H. Xu, D. Dai, Y. Shi, Ultra-Broadband and Ultra-Compact On-Chip Silicon Polarization Beam Splitter by Using Hetero-Anisotropic Metamaterials, Laser and Photonics Reviews 13 (4) (2019) 1800349. doi: https://doi.org/10.1002/lpor.201800349.

[20] M. Ma, A.H.K. Park, Y. Wang, H. Shoman, F. Zhang, N.A.F. Jaeger, L. Chrostowski, Sub-wavelength grating-assisted polarization splitter-rotators for silicon-on-insulator platforms, Opt. Express 27 (13) (2019) 17581–17591, https://doi.org/10.1364/OE.27.017581.

[21] H. Sun, L.R. Chen, Polarization-dependent tuning of bragg reflection enabled through tilted subwavelength grating waveguide bragg gratings, Opt. Lett. 46 (6) (2021) 1450–1453, https://doi.org/10.1364/OL.420412.

[22] H. Xu, D. Dai, Y. Shi, Anisotropic metamaterial-assisted all-silicon polarizer with 415-nm bandwidth, Photon. Res. 7 (12) (2019) 1432–1439, https://doi.org/10.1364/PRJ.7.001432.

[23] P. Cheben, J.H. Schmid, S. Wang, D.-X. Xu, M. Vachon, S. Janz, J. Lapointe, Y. Painchaud, M.-J. Picard, Broadband polarization independent nanophotonic coupler for silicon waveguides with ultra-high efficiency, Opt. Express 23 (17) (2015) 22553, https://doi.org/10.1364/OE.23.022553.

[24] H. Xie, J. Zheng, P. Xu, J. Yao, J. Whitehead, A. Majumdar, Ultra-Compact Subwavelength-Grating-Assisted Polarization-Independent Directional Coupler, IEEE Photon. Technol. Lett. 31 (18) (2019) 1538–1541, https://doi.org/10.1109/LPT.2019.2937890.

[25] Z. Guo, J. Xiao, S. Wu, Ultracompact, polarization-independent, and highly scalable optical power splitting model employing fan-out bending metamaterials, Photon. Res. 10 (11) (2022) 2448–2459, https://doi.org/10.1364/PRJ.470827.

[26] C. Pérez-Armenta, A. Ortega-Moñux, J.M. Luque-González, R. Halir, P.J. Reyes-Iglesias, J. Schmid, P. Cheben, I. Molina-Fernandez, J.G. Wangüemert-Pérez, Polarization-independent multimode interference coupler with anisotropy-engineered bricked metamaterial, Photonics Res. 10 (4) (2022) A57–A65, https://doi.org/10.1364/PRJ.446932.

[27] A. Herrero-Bermello, J.M. Luque-González, R. Halir, P. Cheben, A. Ortega-Moñux, I. Molina-Fernández, A.V. Velasco, Zero-Birefringence Silicon Waveguides Based on Tilted Subwavelength Metamaterials, IEEE Photonics J. 11 (5) (2019) 2700308, https://doi.org/10.1109/JPHOT.2019.2942973.

[28] J.M. Luque-Gonzalez, A. Ortega-Moñux, R. Halir, J.H. Schmid, P. Cheben, I. Molina-Fernandez, J.G. Wangüemert-Pérez, Bricked Subwavelength Gratings: A Tailorable On-Chip Metamaterial Topology, Laser Photonics Rev. 15 (6) (2021) 2000478, https://doi.org/10.1002/lpor.202000478.

[29] R. Halir, I. Molina-Fernández, A. Ortega-Moñux, J.G. Wanguemert-Pérez, D.-X. Xu, P. Cheben, S. Janz, A Design Procedure for High-Performance, Rib-Waveguide-Based Multimode Interference Couplers in Silicon-on-Insulator, J. Lightwave Technol. 26 (16) (2008) 2928–2936, https://doi.org/10.1109/JLT.2007.914511.

[30] S.G. Johnson, J.D. Joannopoulos, Block-iterative frequency-domain methods for Maxwell's equations in a planewave basis, Opt. Express 8 (3) (2001) 173–190, https://doi.org/10.1364/OE.8.000173.

[31] A.F. Oskooi, D. Roundy, M. Ibanescu, P. Bermel, J.D. Joannopoulos, S.G. Johnson, Meep: A flexible free-software package for electromagnetic simulations by the FDTD method, Comput. Phys. Commun. 181 (3) (2010) 687–702, https://doi.org/10.1016/j.cpc.2009.11.008.

[32] H. Shiran, H. Rahbardar Mojaver, J. Bachman, C. Jin, O. Liboiron-Ladouceur, Impact of SiO_2 Cladding Voids in SiPh Building Blocks, in: 2020 IEEE Photonics Conference (IPC), Vancouver, BC, Canada, 2020, pp. 1–2. doi: https://doi.org/10.1109/IPC47351.2020.9252413.

[33] C.J. Stirling, R. Halir, A. Sánchez-Postigo, Z. Qu, J.D. Reynolds, S. Penades, G. S. Murugan, A. Ortega-Moñux, J.G. Wangüemert-Pérez, I. Molina-Fernández, G. Z. Mashanovich, M. Nedeljkovic, Broadband 2 × 2 multimode interference coupler for mid-infrared wavelengths, Opt. Lett. 46 (21) (2021) 5300–5303, https://doi.org/10.1364/OL.439985.